Research Article | Vol. 30, No. 15 / 18 Jul 2022 / Optics Express 27259
Optics EXPRESS

Realization of tunable index-near-zero modes in nonreciprocal magneto-optical heterostructures

YUN ZHOU,[1,2,8] PANPAN HE,[3,8] SANSHUI XIAO,[4] FENGWEN KANG,[4,5,6] LUJUN HONG,[4,7] YUN SHEN,[7] YAMEI LUO,[1,2] AND JIE XU[1,2,*]

[1]School of Medical Information and Engineering, Southwest Medical University, Luzhou 646000, China
[2]Medical Engineering & Medical Informatics Integration and Transformational Medicine of Luzhou Key Laboratory, Luzhou 646000, China
[3]School of Electrical and Electronic Engineering, Luzhou Vocational & Technical College, Luzhou 646000, China
[4]DTU Fotonik, Department of Photonics Engineering, Technical University of Denmark, DK-2800 Kgs. Lyngby, Denmark
[5]Laboratory of Advanced Nano Materials and Devices, Ningbo Institute of Materials Technology and Engineering (NIMTE), Chinese Academy of Sciences (CAS), Ningbo, 315201, China
[6]College of Materials Science and Engineering, Sichuan University, Chengdu 610065, China
[7]Institute of Space Science and Technology, Nanchang University, Nanchang 330031, China
[8]These authors contributed equally to this work
*xujie011451@163.com

Abstract: Epsilon-near-zero (ENZ) metamaterial with the relative permittivity approaching zero has been a hot research topic for decades. The wave in the ENZ region has infinite phase velocity ($v = 1/\sqrt{\varepsilon\mu}$), but it cannot efficiently travel into the other devices or air due to the impedance mismatch or near-zero group velocity. In this paper, we demonstrate that the tunable index-near-zero (INZ) modes with vanishing wavenumbers ($k = 0$) and nonzero group velocities ($v_g \neq \sim 0$) can be achieved in nonreciprocal magneto-optical systems. The INZ modes have been experimentally demonstrated in the photonic crystals at Dirac point frequencies, and that impedance-matching effect has been observed as well [Dubois et al., Nat. Commun. **8**, 14871 (2017)]. Our theoretical analysis reveals that the INZ modes exhibit tunability when changing the parameters of the one-way (nonreciprocal) waveguides. Moreover, owing to the zero-phase-shift characteristic and decreasing v_g of the INZ modes, several perfect optical buffers are proposed in the microwave and terahertz regimes. The theoretical results are further verified by the numerical simulations using the finite element method. Our findings may open new avenues for research in the areas of ultra-strong or -fast nonlinearity, perfect cloaking, high-resolution holographic imaging, and wireless communications.

1. Introduction

Symmetry is common in the natural world. For example, the roads of the incident and reflected light or sound are always symmetric. However, such a common characteristic cannot hold all the time in quantum physics. The chiral edge modes observed in the quantum Hall effect exhibit nonreciprocal propagation properties in opposite directions [1]. Similarly, the one-way electromagnetic (EM) modes are permitted to propagate unidirectionally, and they have been investigated and observed in many physical systems such as the magneto-optical (MO) heterostructure [2–8]. The one-way EM modes in the MO-based structures refer to as unidirectional (one-way) surface magnetoplasmons (SMPs) that are sustained at the surfaces of the MO materials. In 2009, the first experimental realization of unidirectional SMPs was achieved in a photonic crystal (PhC) consisting of yttrium-iron-garnet (YIG) rods [9]. Other

#461237 https://doi.org/10.1364/OE.461237
Journal © 2022 Received 14 Apr 2022; revised 17 Jun 2022; accepted 17 Jun 2022; published 13 Jul 2022

Optics EXPRESS

groups have also explored many interesting phenomena, such as slow light around the exceptional points [10], strong handedness-switchings [11], and broadband field enhancement [12], in the nonreciprocal systems. Recently, the discussion about breaking the time-bandwidth limit by using the MO heterostructure has received much attention. Tsakmakidis et al. claimed that in the MO heterostructure, the time-bandwidth (T-B) limit, which was believed to be a fundamental limit in both engineering and theory, can be overcome due to the broken Lorentz reciprocity [2,13]. Mann et al. challenged such a claim with the coupled-mode theory and argued the causality between the nonreciprocity and breaking the T-B limit [14,15]. Shortly after that, Buddhiraju [16] and Gangaraj [17] et al. proposed that the one-way window of the MO heterostructure may be closed due to the nonlocal effect which is characterized by spatial dispersion. We note here that, in this work we will only consider the local cases because of two reasons: (1) the $k = 0$ modes should not be significantly affected by the nonlocal effect [6,18,19], and (2) the experimental verification of the one-way propagation in the microwave regime guarantees the correctness of the theoretical analysis of the local microwave one-way system [4,9], while the terahertz INZ mode in the nonlocal condition is a novel research topic that we will study in our future work. Besides, our group reported several MO-based one-way nonreciprocal waveguides where many interesting phenomena such as slow wave [20], truly trapping of robust unidirectional rainbow [21,22], and bidirectionally slowed down rainbow trapping and releasing [23] were illustrated. It is inspiring to use the simple powerful MO heterostructure to build novel devices with new functionalities.

Metamaterials (MMs) with fantastic electromagnetic characteristics have been an attractive topic in the past decades. Many different MMs such as negative-index MMs [24,25], hyperbolic metamaterials [26,27], and epsilon-negative MMs [28] were proposed by several research groups. Moreover, the index-near-zero (INZ) MMs, including the epsilon-near-zero (ENZ) MMs with vanishing permittivity [29–32], the μ-near-zero MMs with vanishing permeability [33], double-near-zero (DNZ) MMs with both permittivity and permeability approaching zero [34–36], and the INZ MMs proposed in the PhCs [37,38], is one of the research focus. There are three typical ways to build the ENZ MMs: (1) utilizing the plasma materials such as indium-tin-oxide (ITO) where the ENZ region is always near the plasma frequency [39,40], and (2) building the rectangle waveguide filled with magneto-optical materials while the ENZ region near the cutoff frequency [41], and (3) fabricating layered metal-dielectric configurations, and according to the effective medium theories (EMTs), the real part of the relative permittivity may vanish at discrete frequencies [42]. We note that the group velocities (v_g) in most of the ENZ MMs tend to zero since the imaginary part of the permittivity is negligible as well, leading to forbidden energy transmission [43]. The DNZ MMs were proposed to solve such a problem [34,44,45]. However, both the ENZ and DNZ materials suffer from the narrow operating band and complex manufacturing processes [46]. On the other hand, the INZ materials have wide applications in energy harvesting based on supercoupling effect [39,47], wavefront shaping [34], terahertz lens [32], acoustic MMs or metasurface [48–51], quantum optics [52], switch of total transport, and total reflection [35,53]. We emphasize that even though the experimental realization of the INZ modes has been proposed in all-dielectric systems at Dirac point frequencies [54], it is still of significant interest to dig novel tunable INZ materials with nonzero v_g.

To this end, in what follows, we propose the tunable INZ modes with vanishing wavenumber ($k = 0$) in the simple MO heterostructures. The explored INZ modes are similar to the Dirac point modes illustrated in the PhCs since the effective refractive indices of both the INZ and the Dirac point modes are approaching zero. Moreover, based on our theoretical analysis, the working frequencies of such MO INZ modes can be continually adjusted by modifying the thickness parameters of the structure or the external magnetic field. Therefore, compared to the previously reported INZ modes, our proposed adjustable INZ modes in this work are more favorable in many fields, such as the realization of strong nonlinearity, cloaking, wireless communication,

Optics EXPRESS

and wavefront shaping. As a proof of concept, we further design several microwave and terahertz perfect optical buffers where the EM wave can be slowed down with zero phase shift.

2. Slowed down unidirectional SMPs

In our previous works [20,21,23,55], cutting off the MO material has been proved to be an efficient way to engineer the dispersion of the EM modes (e.g., SMPs) in the nonreciprocal systems. In this paper, we will show how such a technique can be used to achieve the tunable INZ modes. We first study the propagation properties in a metal-dielectric-YIG-metal structure shown in Fig. 1(a). Since the metals can be treated as perfect electric conductors at microwave frequencies, such a configuration is named the 'EDYE'. We note that the dielectric, in this subsection, is set to be air ($\varepsilon_r = 1$). An external magnetic field (H_0) was applied to the YIG layer in the $-z$ direction, and the permeability of YIG, in this case, has the form [56]

$$\vec{\mu}=\begin{bmatrix} \mu_1 & -i\mu_2 & 0 \\ i\mu_2 & \mu_1 & 0 \\ 0 & 0 & 1 \end{bmatrix}, \tag{1}$$

$$\mu_1 = 1 + \frac{\omega_m(\omega_0 - i\nu\omega)}{(\omega_0 - i\nu\omega)^2 - \omega^2}, \mu_2 = \frac{\omega_m\omega}{(\omega_0 - i\nu\omega)^2 - \omega^2}, \tag{2}$$

where ω, ν, ω_0, and ω_m are the angular frequency, the damping coefficient, the precession angular frequency, and the characteristic circular frequency, respectively. $\omega_0 = 2\pi\gamma H_0$ and $\gamma = 2.8 \times 10^6$ rad/s/G is the gyromagnetic ratio. According to Maxwell's equations and the boundary conditions of the EDYE configuration, the dispersion relation of the TE-polarization SMPs can be described by the following equation

$$\alpha_d\mu_v + \alpha_v\frac{\tanh(\alpha_d d_1)}{\tanh(\alpha_v d_2)} + \frac{\mu_2}{\mu_1}k\tanh(\alpha_d d_1) = 0, \tag{3}$$

where d_1 and d_2 are the thicknesses of the dielectric and the YIG layer, respectively. For simplicity, we introduce a thickness parameter $D = (d_1, d_2)$ in this paper. $\alpha_d = \sqrt{k^2 - \varepsilon_r k_0^2}$ and $\alpha_v = \sqrt{k^2 - \varepsilon_m\mu_v k_0^2}$ refer respectively to the attenuation coefficients of SMPs in the dielectric and the YIG layer. We emphasize here that the YIG parameters used in this paper are $\varepsilon_m = 15$ (the permittivity of YIG) and $\omega_m = 2\pi \times 5 \times 10^9$ rad/s ($f_m = 5$ GHz). Owing to the third item of Eq. (3), the propagation characteristics of the EM modes with $k>0$ and $k<0$ are different. As it is well established, the COWP bands in the one-way waveguides are heavily dependent on the asymptotic frequencies (AFs). According to Eq. (3), we can easily calculate the AFs which can be written as follows.

$$\omega_{AF}^{-} = \omega_0 + \frac{\omega_m}{2}, \quad (k \to -\infty) \tag{4}$$

$$\omega_{AF}^{+} = \omega_0 + \omega_m, \quad (k \to +\infty) \tag{5}$$

In Fig.1 (b), two different thickness parameters were considered to show the dispersion properties in the EDSE configurations. The red line indicates the dispersion curve of the SMPs as $D = D_1 = (0.1\lambda_m, 0.15\lambda_m)$ ($\lambda_m = c/f_m \approx 60$ mm, c is the speed of light in vacuum), and $\omega_0 = \omega_m$ ($H_0 \approx 1785.7$G). It is clear that there is a COWP band (the yellow shaded area) which is limited by two AFs, i.e. ω_{AF}^{-} and ω_{AF}^{+}. The gray-colored areas represent the bulk zones of YIG, which are much narrower than the ones in the infinite YIG cases [57], and a new band gap (the cyan zone) emerges below the compressed bulk zone 1. As a contrast, the dashed black line demonstrates the dispersion diagram in a ultra-thin EDYE structure with $D = D_2 = (0.01\lambda_m, 0.01\lambda_m)$. In this

Optics EXPRESS

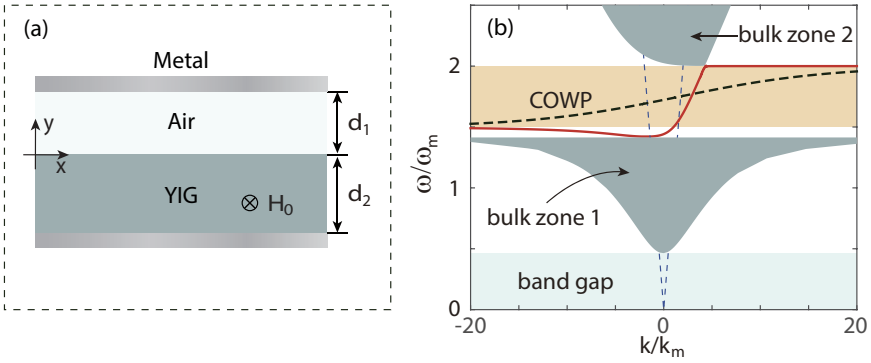

Fig. 1. (a) The schematic of the EDYE model. (b) The dispersion diagrams of SMPs in the metal-dielectric-YIG-metal (EDYE) structure as $D = D_1 = (0.1\lambda_m, 0.15\lambda_m)$ (red line) and $D = D_2 = (0.01\lambda_m, 0.01\lambda_m)$ (dashed black line). The yellow shaded areas indicate the complete one-way propagation (COWP) band while the gray and cyan shaded regions respectively demonstrate the compressed bulk zones and band gaps in the D_1 case. The blue dashed lines are light lines. The other parameters are $\varepsilon_r = 1$, $\omega_0 = \omega_m$, $\varepsilon_m = 15$ and $\omega_m = 2\pi \times 5 \times 10^9$ rad/s.

case, the bandwidth of the COWP band is analogous to the previous one in the D_1 case since the AFs remain the same. We note that the bulk zones 1 and 2 are both narrowed down (not shown in Fig. 1(b)) due to the ultra-thin vertical width [20], and the broadband gap region, which should have potential uses in the design of the optical isolator, is observed as well. The dispersion curve of the SMPs (black line) is much more horizontal than the red one, implying smaller group velocities and slow waves.

To clarify the slow-wave phenomenon occurred in the ultra-thin EDYE structure, we studied two cases of the EDYE structure. In the first case, constant d_2 (= $0.15\lambda_m$) and five different d_1 were considered. The corresponding zoomed-in dispersion diagrams around the COWP region are demonstrated in Fig. 2(a), in which we find that when reducing the thickness of the air layer (d_1), the dispersion branches with k<0 rise up distinctly while most of the dispersion branches in the k>0 region locate near $\omega = \omega_{AF}^{+}$. In the second case, we considered the constant d_1 (= $0.1\lambda_m$) and five different values of d_2, i.e. $0.15\lambda_m$, $0.05\lambda_m$, $0.03\lambda_m$, $0.02\lambda_m$ and $0.1\lambda_m$. The corresponding dispersion diagram is shown in Fig. 2(b) where the dispersion branches with k>0 descend whereas the dispersion branches with k<0 are nearly the same. It is obvious that the group velocities of SMPs decrease when decreasing the value of d_1 (see Fig. 2(a)) or d_2 (see Fig. 2(b)).

More clear results are displayed in Fig. 3, in which the corresponding group velocities and wavenumbers of the SMPs are illustrated in the COWP band $1.5\omega_m$<ω<$2\omega_m$. In Fig. 3(a), we set $d_2 = 0.15\lambda_m$, and the red, the cyan, and the blue solid lines represent the values of v_g in the cases of $d_1 = 0.1\lambda_m$, $d_1 = 0.03\lambda_m$ and $d_1 = 0.01\lambda_m$, respectively. As expected, the solid lines drop down when decreasing the value of d_1. Moreover, similar results are shown in Fig. 3(b) for constant d_1 cases. On the other hand, it is quite different between constant d_2 cases and constant d_1 cases in values of k of the unidirectional modes. As shown in Fig. 3, the dashed lines illustrate the changing of k of the SMPs. In the case of $d_1 = 0.1\lambda_m$, the wavenumbers of SMPs in the COWP band are constantly greater than zero. On the contrary, for $d_2 = 0.15\lambda_m$ case, the wavenumbers can be positive or negative depending on the values of d_2 and frequency. Besides, as demonstrated in Fig. 3(a), the EM modes with $k = 0$ (marked by points) and $v_g \neq 0$, i.e. the index-near-zero (INZ) modes, are found in the EDYE structures. Deriving from Figs. 2 and 3, it is believable that the INZ modes can be manipulated in the whole COWP band by engineering

Optics EXPRESS

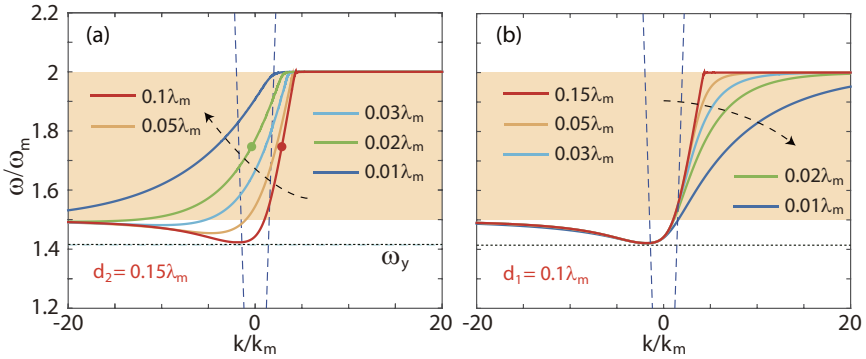

Fig. 2. The relation between the thickness parameter $D = (d_1, d_2)$ and the dispersion curves of SMPs. (a) The dispersion diagrams for five different values of d_1 when $d_2 = 0.15\lambda_m$. (b) The dispersion diagrams for five different values of d_2 when $d_1 = 0.1\lambda_m$.

the thickness of air (d_1). In another word, the EDYE configuration, as discussed above, can support the tunable INZ modes by simply engineering the thickness parameter of the structures. Therefore, due to the slow-wave and tunable characteristics, these simple configurations are promising for designing optical functional devices, and one of its direct uses is designing the perfect optical buffer (POB) with near-zero phase shift. It is also worth noting that varying the external magnetic field, as presented in our previous works, should be another efficient way to engineer the INZ modes [20,22].

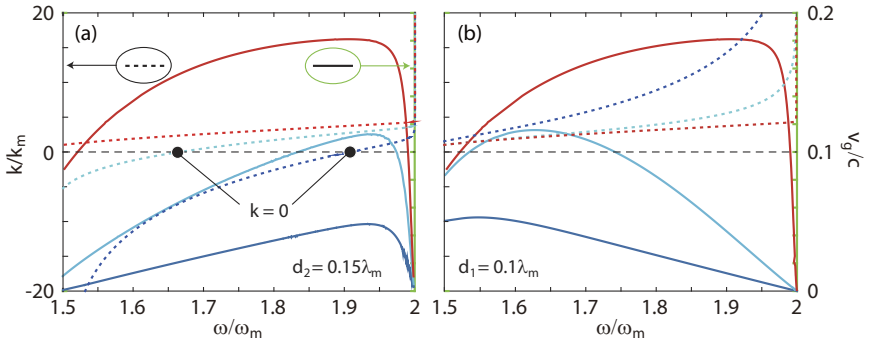

Fig. 3. The wavenumbers (k) and the group velocities (v_g) of SMPs (a) in Fig. 2(a) and (b) in Fig. 2(b) as functions of ω. The solid lines represent the values of v_g whereas the dotted lines show the corresponding values of k. The other parameters are the same as in Fig. 1.

3. Index-near-zero modes and perfect optical buffer

Zero phase shift (ZPS) is an important characteristic in many fields, for example, the near-field radio frequency identification (RFID) applications [58,59]. In this subsection, we will propose the two-dimensional (2D) and three-dimensional (3D) POBs in the microwave regime based on the EDYE configuration. The inset of Fig. 4(a) indicates the simulated magnetic field (E_z) in a thick-thin straight EDYE waveguide as $f = 1.75f_m$ and $\nu = 10^{-3}\omega$ (the damping coefficient). The thickness parameters for the thick and thin parts are $D = D_1 = (0.1\lambda_m, 0.15\lambda_m)$ and $D = D_3 = (0.02\lambda_m, 0.15\lambda_m)$, respectively, and two parts have the same length of $L_1 = L_2 = 60$ mm. We note here that the simulations were performed by utilizing the finite element method

Optics EXPRESS

(FEM), and the lossy MO materials were considered in all simulations, with the aim of illustrating the loss effects on the nonreciprocity and the INZ characteristics. In the simulations, the EM mode was excited by a line current source at $x = 20$ mm in the thick part, and it propagated along the air-YIG interface with the phase angle (Φ) of E_z changing in the $[-\pi, \pi]$ region. Once the wave reaches and further transmits into the thin EDYE part, the curve (blue solid line in Fig. 4(a)) of Φ of E_z becomes gentle since $|k|$ of the SMPs in the thick part is larger than the one in the thin part (see points in Fig. 2). It is quite inspiring to manipulate the phase-angle curve and to further make it nearly horizontal because the horizontal curve implies ZPS. In Fig. 4(b), d_1 is slightly enlarged, and we set $D = D_4 = (0.0216\lambda_m, 0.15\lambda_m)$. In this case, Φ remains almost unchanged in the thin part except for the area near the rightmost end (PEC wall) of the waveguide. Since the EM wave can be slowed down with ZPS in the thin part, the structure demonstrated in the inset of Fig. 4(b) is suitable for the design of the POB. We note here that, in our previous work we have shown that the surface wave located in the light cone can efficiently couple with the fundamental modes of traditional dielectric waveguide [3]. Therefore, the above-mentioned INZ modes are promising in many fields, such as wireless communication and optical cloaking.

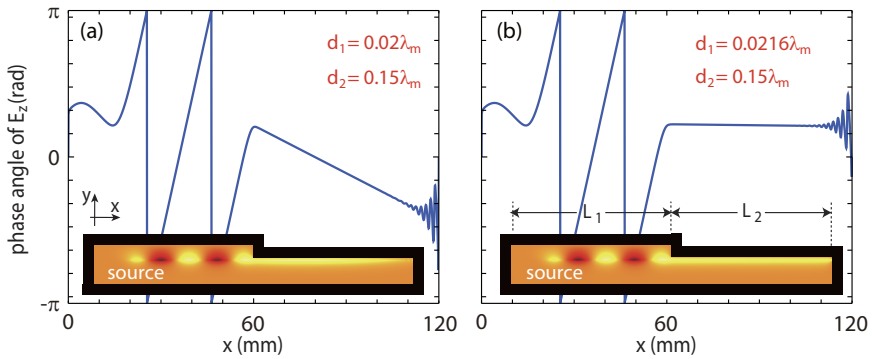

Fig. 4. The phase angle (Φ) of E_z along the air-YIG interface in the finite element method (FEM) simulations for (a) $D = D_3 = (0.02\lambda_m, 0.15\lambda_m)$, and (b) $D = D_4 = (0.0216\lambda_m, 0.15\lambda_m)$. The insets show the electric-field (E_z) distributions in the simulations where the structures are surrounded by PEC walls (the black areas). The other parameters are $f = 1.75f_m$, $L_1 = L_2 = 60$ mm and $\nu = 10^{-3}\omega$.

To further explore the POB theory based on the EDYE configuration, the frequencies (ω) of the INZ modes are plotted as a function of d_1 for three different d_2, and the results are shown in Fig. 5(a). As one can see, the black star is on the red line which indicates the case of $d_2 = 0.15\lambda_m$, and the corresponding frequency $\omega = 1.75\omega_m$ while $d_1 \approx 0.0216\lambda_m$. Thus, our calculation fits well with the simulation results illustrated in Fig. 4(b). The green and blue lines indicate the cases of smaller d_2, i.e. $d_2 = 0.02\lambda_m$ and $d_2 = 0.01\lambda_m$. It is obvious that when decreasing d_2, the line drops down, which implies the decreasing ω of the INZ modes. One can derive the same conclusion from Fig. 2(b), in which the dispersion curve drops down when decreasing d_2. Noteworthily, the INZ region can be efficiently varied in the COWP band by modifying the thickness parameter while the COWP band can be tuned by changing the external magnetic field [60]. The INZ modes/region mentioned here can be dynamically switched from 'on' to 'off' by controlling the external magnetic field. In this work, we just focus on the cases of the stable external magnetic field. Based on the above results, we further designed a complete POB consisting of three straight EDYE parts. As shown in the inset of Fig. 5(b), the values of d_1 in the three parts are $d_1 = 0.1\lambda_m$, $d_1 = 0.039\lambda_m$ and $d_1 = 0.1\lambda_m$, respectively. In the simulation, we set the operating frequency (f) to be $1.6f_m$ (red star in Fig. 5(a)). As shown in Fig. 5(b), the launched wave transmits through the second part and recovers in the third part, and the phase angle of the

Optics EXPRESS

wave is nearly unchanged during the propagation process in the second part. Due to the coupling effect between the modes in the thick and thin parts, a slight phase shift is found at the thick-thin interfaces (see the upper inset of Fig. 5(b)). An efficient way to reduce the coupling effect is to add a tapered EDYE configuration between the thick and thin EDYE parts. Figure 5(c) shows the designed thick-tapered-thin (TTT) EDYE structure. In the simulations of the TTT structure (Fig. 5(c), lower panel), we find that the effective wavelength (λ_{ef}) is gradually lengthened along the $+x$ direction in the tapered part, and λ_{ef} tends to be near-infinite in the ultra-thin part. More importantly, the phase shift induced by the propagation in the ultra-thin part can be less than $0.3\%\Phi_0$ (Φ_0 is the incident phase angle) when $L_2 = 3L_1 = 180$ μm.

The 2D POB theory based on the EDYE configuration can also be used to design realistic 3D POBs. The schematic of a designed 3D POB, which is also constructed by three EDYE parts, is shown in Fig. 6, and the direction of the external magnetic field is assumed to be $-z$. According to the analysis of Figs. 2 and 3, both the air and YIG layers of the thin part of the 3D POB are designed to be narrower than the thick parts to efficiently slow the wave, which is different from the above 2D POB. As an example, the thickness parameters in the three parts of the 3D POB are set respectively to be $D = D_6 = (0.05\lambda_m, 0.15\lambda_m)$, $D = D_7 = (0.01452\lambda_m, 0.02\lambda_m)$ (marked by the green star in Fig. 5(a)) and $D = D_6$, and we further performed the FEM simulation in such a 3D EDYE structure. As shown in Fig. 7(a) and the inset of Fig. 7(b), similar to the 2D simulations presented in Figs. 4 and 5, the wave unidirectionally propagates from the first thick part and travels through the ultra-thin part and is trapped in the rightmost end of the last part. Figure 7(b) demonstrates the changing of the phase angle of the wave along $y = d_{10}/2$ (d_{10}, the air thickness in the thin part) in the XY plane ($z = w/2$ where w is the lateral thickness of the structure). As expected, the clear ZPS is also observed in the thin part of such a 3D one-way waveguide. In a sense, our designed microwave POB can also work as a type of cloaking device since the INZ wave travels through the structure with ZPS and without reflection.

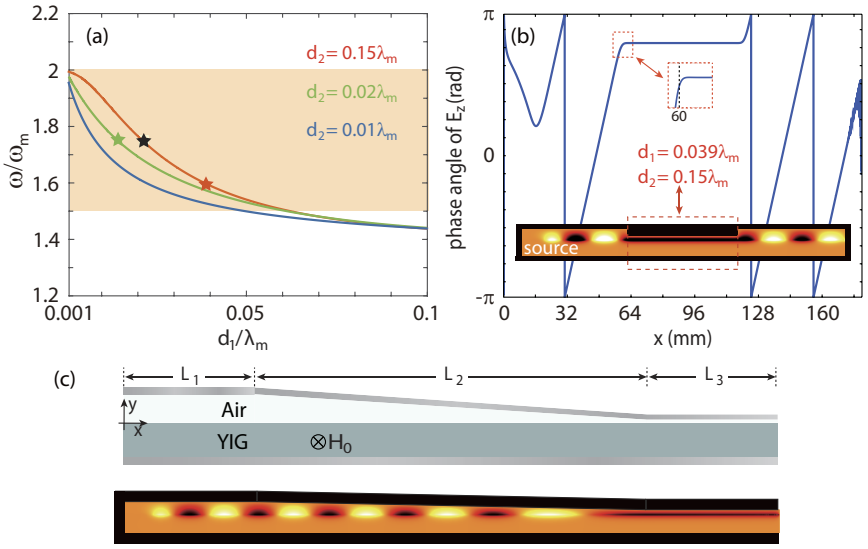

Fig. 5. (a) Theory of the tunable POB based on the EDYE configuration. Solid lines illustrate the numerical solutions of $k = 0$ when $d_2 = 0.15\lambda_m$ (red line), $d_2 = 0.02\lambda_m$ (green line) and $d_2 = 0.01\lambda_m$ (blue line), respectively. (b) The phase angle of E_z along the air-YIG interface in a microwave POB for $f = 1.6f_m$. The thickness parameter in the compressing part is $D = D_5 = (0.039\lambda_m, 0.15\lambda_m)$ (red star in (a)). The inset illustrates the distribution of simulated E_z. (c) The schematic and the FEM simulation of a tapered EDYE structure.

Optics EXPRESS

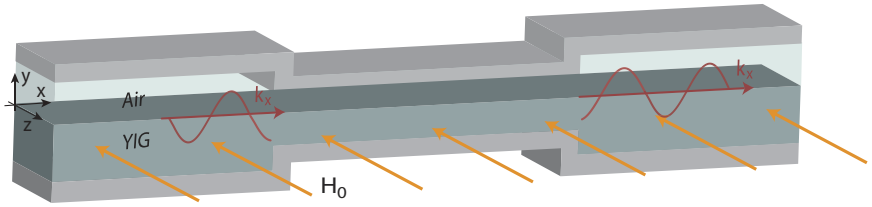

Fig. 6. The schematic of a three-dimensional (3D) POB.

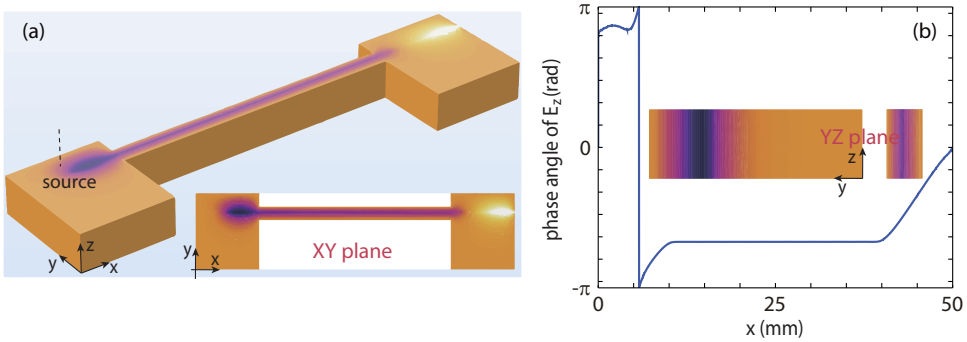

Fig. 7. (a) Simulated electric-field distribution in a 3D POB where the thickness parameters of the thick and thin parts are respectively $D = D_6 = (0.05\lambda_m, 0.15\lambda_m)$ and $D = D_7 = (0.01452\lambda_m, 0.02\lambda_m)$. The inset illustrates the distribution of E_z in XY plane ($z = w/2$) and the inset of (b) shows the corresponding distribution of E_z in YZ planes (Left: $x = 7$ mm. Right: $x = 17$ mm.). (b) The phase angle of E_z along the interface of the XY plane ($z = w/2$) and the XZ plane ($y = d_{10}/2$).

4. INZ mode-based POB in the terahertz regime

Nowadays, communication band gradually transfers from microwave to terahertz regime due to the increase in demand for enormous information. It is really meaningful to extend the microwave POB theory to the terahertz regime. As we reported in previous works [20,21,23], the COWP band may narrow down or vanish in sub-wavelength one-way terahertz waveguides. Moreover, to our knowledge, the INZ modes have never been reported in the one-way terahertz waveguide sandwiched by metals. In this subsection, we propose two types of terahertz POB utilizing the perfect magnetic conductor (PMC) boundary. As shown in Fig. 8, the leftmost two diagrams indicate the two kinds of one-way terahertz waveguides, and the upper one is the PMC-dielectric-semiconductor-PEC (MDSE) structure, while the lower one is the PMC-dielectric-semiconductor-PMC (MDSM) structure. Here, we note that the dielectric layers applied in the MDSE and MDSM waveguides are air and silicon, respectively, for engineering appropriate COWP bands. We emphasize that the PEC-dielectric-semiconductor-PEC (EDSE) and PEC-dielectric-semiconductor-PMC (EDSM) structures cannot sustain the INZ modes, and thus they were not considered in designing the terahertz POB. The dispersion relation of TM-polarization SMPs in the MDSE and MDSM structures can be derived by solving Maxwell's equations, and they have the following forms

$$\left(k^2 - \varepsilon_1 k_0^2\right)\tanh(\alpha d_2) + \frac{\varepsilon_1}{\varepsilon_d}\alpha_d\left[\alpha - \frac{\varepsilon_2}{\varepsilon_1}k\tanh(\alpha d_2)\right]\frac{1}{\tanh(\alpha_d d_1)} = 0, \quad \text{(MDSE)} \tag{6}$$

$$\frac{\varepsilon_2}{\varepsilon_1}k + \frac{\alpha}{\tanh(\alpha d_2)} + \frac{\varepsilon_v}{\varepsilon_d}\frac{\alpha}{\tanh(\alpha_d d_1)} = 0, \quad \text{(MDSM)} \tag{7}$$

Optics EXPRESS

where $\varepsilon_1 = \varepsilon_\infty \left\{1 - \frac{(\omega+i\nu)\omega_p^2}{\omega\left[(\omega+i\nu)^2-\omega_c^2\right]}\right\}$, $\varepsilon_2 = \varepsilon_\infty \frac{\omega_c\omega_p^2}{\omega\left[(\omega+i\nu)^2-\omega_c^2\right]}$ and $\varepsilon_v = \varepsilon_1 - \frac{\varepsilon_2^2}{\varepsilon_1}$. ε_∞, ν, ω_p and $\omega_c = \frac{eH_0}{m^*}$ are the high-frequency permittivity, the electron scattering frequency, the plasma frequency and the electron cyclotron frequency of the semiconductor, respectively. ε_d, α and α_d are the relative permittivity of the dielectric, the attenuation coefficient in the semiconductor and the attenuation coefficient in the dielectric, respectively. The semiconductor in this paper is assumed to be N-type InSb with $\omega_p = 4\pi \times 10^{12}$ rad/s and $\varepsilon_\infty = 15.6$. The asymptotic frequency (AF) is one of the important keys in the study of the one-way waveguide. By solving Eqs. (6) and (7), we find three AFs in the MDSE model and four AFs in the MDSM model. The AFs in the MDSE structure can be written as

$$\begin{cases} \omega_{AF}^{(1)} = \omega_c \\ \omega_{AF}^{(2)} = \omega_{sp}^{(1)} = \frac{1}{2}\left(\sqrt{\omega_c^2 + \frac{4\varepsilon_\infty}{\varepsilon_\infty+\varepsilon_{d1}}\omega_p^2} - \omega_c\right) \\ \omega_{AF}^{(3)} = \omega_{sp}^{(2)} = \frac{1}{2}\left(\sqrt{\omega_c^2 + \frac{4\varepsilon_\infty}{\varepsilon_\infty+\varepsilon_{d1}}\omega_p^2} + \omega_c\right) \end{cases} \tag{8}$$

while the AFs in the MDSM structures are found to be

$$\begin{cases} \omega_{AF}^{(1)} = \omega_{sp}^{(1)} = \frac{1}{2}\left(\sqrt{\omega_c^2 + \frac{4\varepsilon_\infty}{\varepsilon_\infty+\varepsilon_{d2}}\omega_p^2} - \omega_c\right) \\ \omega_{AF}^{(2)} = \omega_a = \frac{1}{2}\left(\sqrt{\omega_c^2 + 4\omega_p^2} - \omega_c\right) \\ \omega_{AF}^{(3)} = \omega_{sp}^{(2)} = \frac{1}{2}\left(\sqrt{\omega_c^2 + \frac{4\varepsilon_\infty}{\varepsilon_\infty+\varepsilon_{d2}}\omega_p^2} + \omega_c\right) \\ \omega_{AF}^{(4)} = \omega_b = \frac{1}{2}\left(\sqrt{\omega_c^2 + 4\omega_p^2} + \omega_c\right) \end{cases} \tag{9}$$

$\varepsilon_{d1} = 1$ and $\varepsilon_{d2} = 11.68$ are the relative permittivities of air and silicon, respectively.

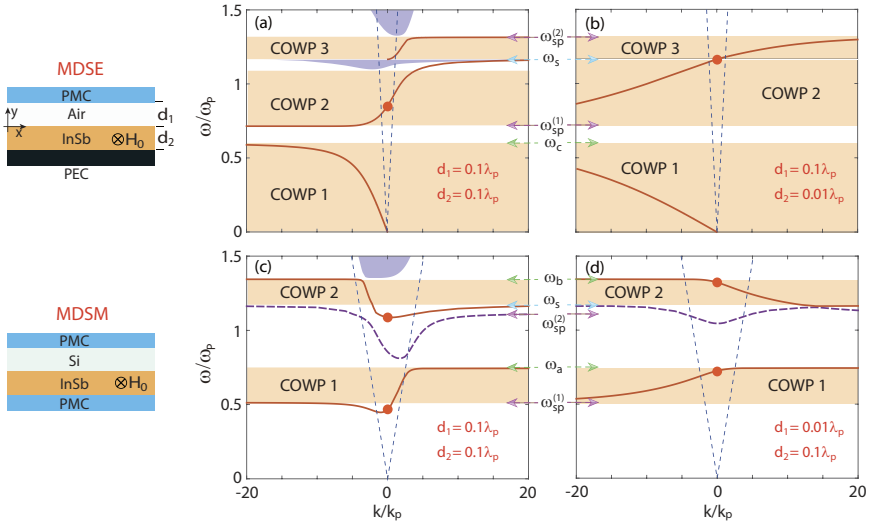

Fig. 8. Realization of the terahertz POB by utilizing PMC walls. The dispersion diagrams of PMC-air-InSb-PEC (MDSE) structures as (a) $D = D_8 = (d_1, d_2) = (0.1\lambda_p, 0.1\lambda_p)$ and (b) $D = D_9 = (0.1\lambda_p, 0.01\lambda_p)$. (c) and (d) demonstrate the dispersion diagrams of PMC-air-InSb-PMC (MDSM) structures as $D = D_8$ and $D = D_{10} = (0.01\lambda_p, 0.1\lambda_p)$, respectively. Two leftmost diagrams show the schematics of the MDSE and MDSM configurations. The other parameters are $\varepsilon_{d1} = 1$, $\varepsilon_{d2} = 11.68$, $\varepsilon_\infty = 15.6$ and $\omega_c = 0.6\omega_p$.

Optics EXPRESS

Figure 8(a) shows the dispersion curves of SMPs in the MDSE structure as $D = D_8 = (0.1\lambda_p, 0.1\lambda_p)$ (λ_p = 150 mum) and $\omega_c = 0.6\omega_p$. It is clear that there are three discrete COWP bands, and three corresponding AFs are $\omega_{AF}^{(1)} = 0.6\omega_p$, $\omega_{AF}^{(2)} \approx 0.71\omega_p$ and $\omega_{AF}^{(3)} \approx 1.31\omega_p$. The bulk zones are significantly compressed in this case, making a remarkable total bandwidth of the COWP bands. Moreover, a terahertz INZ mode (marked by a red point) with $k = 0$ is found in the COWP 2 region. When further decreasing the thickness of InSb, as shown in Fig. 8(b) where $D = D_9 = (0.1\lambda_p, 0.01\lambda_p)$, the bulk zones nearly disappear in the $[0, 1.5\omega_p]$ band. Furthermore, the SMPs sustained at the air-InSb and PEC-InSb interfaces strongly coupled with each other when $\omega \approx \omega_s$ ($\omega_s = \sqrt{\omega_c^2 + \omega_p^2}$), leading to the connecting dispersion curve (the upper red line). Besides, compared to the INZ mode in Fig. 8(a), the one in Fig. 8(b) rise up, which implies the higher working frequency of the one-way INZ mode. We further plotted the dispersion diagrams of the MDSM structures for $D = D_8 = (0.1\lambda_p, 0.1\lambda_p)$ (Fig. 8(c)) and $D = D_{10} = (0.01\lambda_p, 0.1\lambda_p)$ (Fig. 8(d)) as $\omega_c = 0.6\omega_p$. Four AFs in this condition are $\omega_{AF}^{(1)} \approx 0.51\omega_p$, $\omega_{AF}^{(2)} \approx 0.74\omega_p$, $\omega_{AF}^{(3)} \approx 1.11\omega_p$ and $\omega_{AF}^{(4)} \approx 1.34\omega_p$, respectively. As shown in Figs. 8(c) and 8(d), there are two COWP bands in which the EM waves have opposite propagation directions. More interestingly, the INZ modes can be found in all COWP bands once we carefully design the thickness of silicon (Fig. 8(d)). Since the INZ modes in the MDSE and MDSM waveguides have been observed and the INZ mode has been proved to be capable of being manipulated by changing the thickness of the semiconductor or the dielectric, we believe the tunable terahertz POBs can be achieved based on such two configurations.

In order to further demonstrate the relation between the INZ modes and the thickness parameters, we plotted ω as a function of d_2 for the MDSE waveguide with $d_1 = 0.1\lambda_p$, as depicted in Fig. 9(a). As expected, the unidirectional INZ modes are found in a broad band within the COWP band. Note that the upper limit of the COWP band in Fig. 9(a) represents the cut-off frequency (ω_{cf}) of the lower bulk zone (see Fig. 8(a)). For the MDSM configuration, two kinds of INZ modes, i.e. the higher and the lower INZ modes (see Figs. 8(c,d)), were studied. Consequently, the INZ modes are tunable in almost the entire COWP bands. Based on the above results, we designed three types of terahertz POBs which are named the type-1, type-2, and type-3 POBs, respectively. The schematics of these POBs are exhibited at the top of Fig. 10. The thickness parameters of the thin parts of three POBs are $D = D_{11} = (0.1\lambda_p, 0.05596\lambda_p)$ (the vertical line in Fig. 9(a)), $D = D_{12} = (0.0561\lambda_p, 0.1\lambda_p)$ (the vertical line in Fig. 9(b)) and $D = D_{13} = (0.02945\lambda_p, 0.1\lambda_p)$ (the vertical line in Fig. 9(c)), respectively. The simulated magnetic field H_z of three thick-thin-thick waveguides are shown in the insets of Fig. 10, and the working frequencies were $f = f_p, f = 0.6f_p$ and $f = 1.25f_p$, respectively. One should note that in the last simulation (Fig. 10(c)), the external magnetic field was reversed (see the top diagram of Fig. 10(c)) to support the forward-propagating (+x) EM wave. The lossy InSb with $\nu = 0.001$ were considered in the FEM simulations to study the loss effect on the one-way INZ modes. The propagation properties of the launched EM waves in the simulations are similar to those in the microwave simulations (e.g. Figure 5(b)) demonstrated in the last subsections. Moreover, the phase angles remain the same in the thin parts of the three structures, which are in agreement with the calculation results illustrated in Fig. 9. Therefore, we conclude that the loss in the terahertz POBs will not significantly affect the propagation properties of the EM modes such as the INZ modes, and a similar result has been demonstrated in the INZ MMs with cylindrical defects [35]. Finally, according to our simulations, the transmission efficiencies of the INZ modes in the microwave/terahertz POBs can be more than 85%. This high-performance characteristic is due to the 'topologically' unidirectional propagation properties in our design POBs [13], whereas the supercoupling transmission suggested in other ENZ/INZ structures always require ultra-small electrical scale(s) [29,47].

Optics EXPRESS

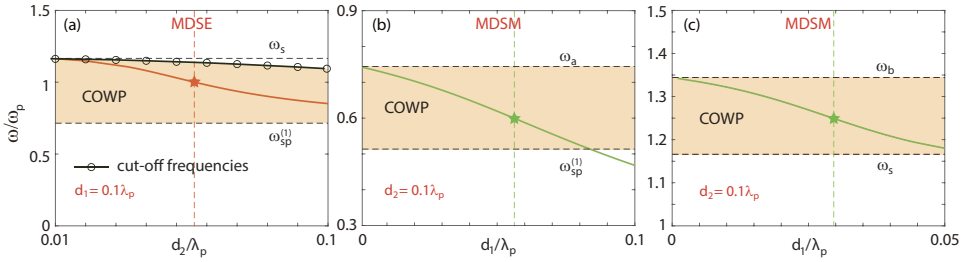

Fig. 9. (a) The frequencies of the INZ modes in the MDSE waveguides as a function of d_2 as $d_1 = 0.1\lambda_p$. The frequencies of (b) the lower INZ modes and (c) the upper INZ modes in the MDSM waveguides as functions of d_1 as $d_2 = 0.1\lambda_p$. The other parameters are the same as in Fig. 8.

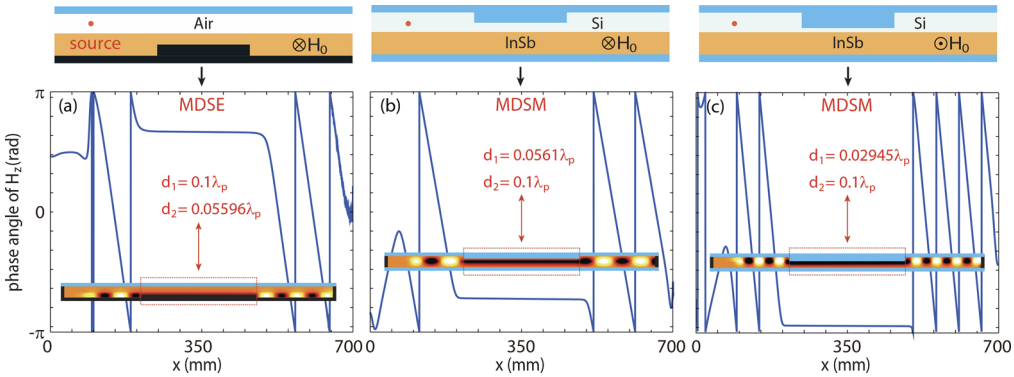

Fig. 10. The phase angle of H_z along the dielectric-InSb interface in (a) MDSE-based and (b,c) MDSM-based terahertz POBs. The thickness parameters of the thin parts of the POBs are respectively (a) $D = D_{11} = (0.1\lambda_p, 0.05596\lambda_p)$, (b) $D = D_{12} = (0.0561\lambda_p, 0.1\lambda_p)$ and (c) $D = D_{13} = (0.02945\lambda_p, 0.1\lambda_p)$. The operating frequencies in the simulations are $f = f_p$, $f = 0.6f_p$ and $f = 1.25f_p$ in sequence. The InSb is considered to be lossy in the simulations with electron scattering frequency $\nu = 0.001$.

We emphasize here that the INZ mode in this work is related to the single unidirectional mode, implying the single-zero effective permeability in the microwave MO systems and the single-zero effective permittivity in the terahertz MO systems, which is different from the INZ mode in the DNZ media based on PhCs with Dirac-like cones that are 3-fold degeneracies at the Dirac points [61–63]. Moreover, the INZ modes in the DNZ systems always suffer from the half-wavelength scale and the opposite-sign group velocities at the Dirac point frequency, whereas our proposed MO INZ modes can work even in the deep-subwavelength system due to the robust unidirectionality, which may pave the route to ultra-compact optical communication. Furthermore, the MO INZ mode, because of the tunability, is with significant advantages compared to the one in the PhCs. On the other hand, one should also note that similar single-zero characteristics, e.g. near-zero effective permittivity and non-zero effective permeability, have been proposed in some works by using complicated techniques/devices such as photonic doping [64], metamaterial [65], and strong-coupling system [41]. Meanwhile, because of the reciprocity, there are at least two group velocities in the ENZ region of these systems. On the contrary, the MO INZ modes in this work are achieved relied on simple waveguide systems, and only a single group velocity is found at the specific INZ frequency.

Optics EXPRESS

5. Conclusion

We have studied the tunable index-near-zero (INZ) modes in simple MO heterostructures. As an example of the potential applications of the INZ modes, we have further proposed the low-loss microwave POBs and terahertz POBs. In the microwave regime, we have demonstrated that by carefully modifying the thickness (d_1) of the dielectric layer, the INZ modes can be tuned in a broad band (i.e. the COWP band). The group velocities v_g of the INZ modes were found to be nonzero, and v_g decreased when decreasing d_1, indicating the slowed wave in the thin MO structures. The slow-wave and tunable characteristics of the microwave INZ modes have been confirmed by the numerical simulations of the POBs.

In addition, we have extended our research to the terahertz regime. By using the PMC wall(s), three types of terahertz INZ mode-based POBs have been proposed based on the MDSE and the MDSM configurations. Moreover, the terahertz INZ mode, according to our analysis, is different from the microwave INZ mode. More specifically, the terahertz INZ mode can be engineered by changing the thickness of the semiconductor in the MDSE structure or by changing the thickness of the dielectric in the MDSM structure. We have also proposed a promising way to turn 'on' or 'off' the INZ region by easily varying the external magnetic field, making our MO materials-based INZ modes highly maneuverable in practice. Owing to the characteristics of one-way propagation, ZPS, and tunability, the microwave and terahertz INZ modes in the simple MO heterostructures have great potential for high-performance and directional wireless communication, cloaking, holographic imaging, and other optical functional devices in integrated optical communication besides POBs.

Funding. National Natural Science Foundation of China (61865009, 61927813); Funding of Southwest Medical University (20/00160222); Department of Science and Technology of Sichuan Province (14JC0153); Science and Technology Strategic Cooperation Programs of Luzhou Municipal People's Government and Southwest Medical University (2019LZXNYDJ18); Horizon 2020 Framework Programme (713683); the Spring Buds Program from NIMTE CAS starting grant; The open fund of Chongqing Key Laboratory of Photo-Electric Functional Materials (K[2022]206).

Disclosures. The authors declare that there are no conflicts of interest related to this article.

Data availability. No data were generated or analyzed in the presented research.

References

1. R. E. Prange and S. M. Girvin, *The Quantum Hall effect* (Springer, 1987).
2. K. L. Tsakmakidis, L. Shen, S. A. Schulz, X. Zheng, J. Upham, X. Deng, H. Altug, A. F. Vakakis, and R. W. Boyd, "Breaking lorentz reciprocity to overcome the time-bandwidth limit in physics and engineering," Science **356**(6344), 1260–1264 (2017).
3. L. Shen, J. Xu, Y. You, K. Yuan, and X. Deng, "One-way electromagnetic mode guided by the mechanism of total internal reflection," IEEE Photonics Technol. Lett. **30**(2), 133–136 (2017).
4. M. Wang, R.-Y. Zhang, L. Zhang, D. Wang, Q. Guo, Z.-Q. Zhang, and C. T. Chan, "Topological one-way large-area waveguide states in magnetic photonic crystals," Phys. Rev. Lett. **126**(6), 067401 (2021).
5. S. A. H. Gangaraj and F. Monticone, "Coupled Topological Surface Modes in Gyrotropic Structures: Green's Function Analysis," IEEE Antennas Wirel. Propag. Lett. **17**(11), 1993–1997 (2018).
6. S. A. H. Gangaraj, G. W. Hanson, M. G. Silveirinha, K. Shastri, M. Antezza, and F. Monticone, "Unidirectional and diffractionless surface plasmon polaritons on three-dimensional nonreciprocal plasmonic platforms," Phys. Rev. B **99**(24), 245414 (2019).
7. S. Pakniyat, A. M. Holmes, G. W. Hanson, S. A. H. Gangaraj, M. Antezza, M. G. Silveirinha, S. Jam, and F. Monticone, "Non-Reciprocal, Robust Surface Plasmon Polaritons on Gyrotropic Interfaces," IEEE Trans. Antennas Propag. **68**(5), 3718–3729 (2020).
8. L. Hong, Y. Wang, Y. Shen, X. Deng, K. Yuan, S. Xiao, and J. Xu, "Broadband energy squeezing and tunneling based on unidirectional modes," Opt. Mater. Express **11**(9), 2975–2984 (2021).
9. Z. Wang, Y. Chong, J. D. Joannopoulos, and M. Soljačić, "Observation of unidirectional backscattering-immune topological electromagnetic states," Nature **461**(7265), 772–775 (2009).
10. S. A. H. Gangaraj and F. Monticone, "Topological Waveguiding near an Exceptional Point: Defect-Immune, Slow-Light, and Loss-Immune Propagation," Phys. Rev. Lett. **121**(9), 093901 (2018).
11. M. Alidoust and K. Halterman, "Controllable nonreciprocal optical response and handedness-switching in magnetized spin-orbit coupled graphene," Phys. Rev. B **105**(4), 045409 (2022).
12. S. A. H. Gangaraj, B. Jin, C. Argyropoulos, and F. Monticone, "Broadband field enhancement and giant nonlinear effects in terminated unidirectional plasmonic waveguides," Phys. Rev. Appl. **14**(5), 054061 (2020).

Optics EXPRESS

13. K. L. Tsakmakidis, Y. You, T. Stefański, and L. Shen, "Nonreciprocal cavities and the time-bandwidth limit: comment," Optica **7**(9), 1097–1101 (2020).
14. S. A. Mann, D. L. Sounas, and A. Alù, "Nonreciprocal cavities and the time–bandwidth limit," Optica **6**(1), 104–110 (2019).
15. S. A. Mann, D. L. Sounas, and A. Alù, "Nonreciprocal cavities and the time-bandwidth limit: Reply," Optica **7**(9), 1102–1107 (2020).
16. S. Buddhiraju, Y. Shi, A. Song, C. Wojcik, M. Minkov, I. A. D. Williamson, A. Dutt, and S. Fan, "Absence of unidirectionally propagating surface plasmon-polaritons at nonreciprocal metal-dielectric interfaces," Nat. Commun. **11**(1), 674 (2020).
17. S. A. H. Gangaraj and F. Monticone, "Do truly unidirectional surface plasmon-polaritons exist?" Optica **6**(9), 1158–1165 (2019).
18. S. A. H. Gangaraj and F. Monticone, "Physical violations of the bulk-edge correspondence in topological electromagnetics," Phys. Rev. Lett. **124**(15), 153901 (2020).
19. K. L. Tsakmakidis, K. Baskourelos, and T. Stefański, "Topological, nonreciprocal, and multiresonant slow light beyond the time-bandwidth limit," Appl. Phys. Lett. **119**(19), 190501 (2021).
20. J. Xu, S. Xiao, C. Wu, H. Zhang, X. Deng, and L. Shen, "Broadband one-way propagation and rainbow trapping of terahertz radiations," Opt. Express **27**(8), 10659–10669 (2019).
21. J. Xu, P. He, D. Feng, K. Yong, L. Hong, Y. Shen, and Y. Zhou, "Slow wave and truly rainbow trapping in a one-way terahertz waveguide," Opt. Express **29**(7), 11328–11341 (2021).
22. J. Xu, S. Xiao, P. He, Y. Wang, Y. Shen, L. Hong, Y. Luo, and B. He, "Realization of broadband truly rainbow trapping in gradient-index metamaterials," Opt. Express **30**(3), 3941–3953 (2022).
23. J. Xu, Q. Shen, K. Yuan, X. Deng, Y. Shen, H. Zhang, C. Wu, S. Xiao, and L. Shen, "Trapping and releasing bidirectional rainbow at terahertz frequencies," Opt. Commun. **473**, 125999 (2020).
24. D. R. Smith, J. B. Pendry, and M. C. Wiltshire, "Metamaterials and negative refractive index," Science **305**(5685), 788–792 (2004).
25. Y. Yang, Y. Ge, R. Li, X. Lin, D. Jia, Y.-J. Guan, S.-Q. Yuan, H.-X. Sun, Y. Chong, and B. Zhang, "Demonstration of negative refraction induced by synthetic gauge fields," Sci. Adv. **7**(50), eabj2062 (2021).
26. P. Huo, S. Zhang, Y. Liang, Y. Lu, and T. Xu, "Hyperbolic metamaterials and metasurfaces: Fundamentals and applications," Adv. Opt. Mater. **7**(14), 1801616 (2019).
27. J. Li, G. Hu, L. Shi, N. He, D. Li, Q. Shang, Q. Zhang, H. Fu, L. Zhou, W. Xiong, J. Guan, J. Wang, S. He, and L. Chen, "Full-color enhanced second harmonic generation using rainbow trapping in ultrathin hyperbolic metamaterials," Nat. Commun. **12**(1), 6425 (2021).
28. Q. He, K. Sun, Z. Wang, Z. Wang, P. Yang, J. Tian, W. Duan, and R. Fan, "Epsilon-negative behavior and its capacitance enhancement effect on trilayer-structured polyimide-silica/multiwalled carbon nanotubes/polyimide-polyimide composite," J. Mater. Chem. C **10**(11), 4286–4294 (2022).
29. M. Silveirinha and N. Engheta, "Tunneling of Electromagnetic Energy through Subwavelength Channels and Bends using ε -Near-Zero Materials," Phys. Rev. Lett. **97**(15), 157403 (2006).
30. Y. Zhou, M. Z. Alam, M. Karimi, J. Upham, O. Reshef, C. Liu, A. E. Willner, and R. W. Boyd, "Broadband frequency translation through time refraction in an epsilon-near-zero material," Nat. Commun. **11**(1), 2180 (2020).
31. A. R. Davoyan, A. M. Mahmoud, and N. Engheta, "Optical isolation with epsilon-near-zero metamaterials," Opt. Express **21**(3), 3279–3286 (2013).
32. V. Torres, V. Pacheco-Pe na, P. Rodríguez-Ulibarri, M. Navarro-Cía, M. Beruete, M. Sorolla, and N. Engheta, "Terahertz epsilon-near-zero graded-index lens," Opt. Express **21**(7), 9156–9166 (2013).
33. J. S. Marcos, M. G. Silveirinha, and N. Engheta, "μ -near-zero supercoupling," Phys. Rev. B **91**(19), 195112 (2015).
34. R. W. Ziolkowski, "Propagation in and scattering from a matched metamaterial having a zero index of refraction," Phys. Rev. E **70**(4), 046608 (2004).
35. V. C. Nguyen, L. Chen, and K. Halterman, "Total Transmission and Total Reflection by Zero Index Metamaterials with Defects," Phys. Rev. Lett. **105**(23), 233908 (2010).
36. C. Xu, M. Farhat, and Y. Wu, "Non-Hermitian electromagnetic double-near-zero index medium in a two-dimensional photonic crystal," Appl. Phys. Lett. **119**(22), 224102 (2021).
37. X. Huang, Y. Lai, Z. H. Hang, H. Zheng, and C. T. Chan, "Dirac cones induced by accidental degeneracy in photonic crystals and zero-refractive-index materials," Nat. Mater. **10**(8), 582–586 (2011).
38. X. Huang, M. Xiao, Z.-Q. Zhang, and C. T. Chan, "Sufficient condition for the existence of interface states in some two-dimensional photonic crystals," Phys. Rev. B **90**(7), 075423 (2014).
39. N. Engheta, "Pursuing Near-Zero Response," Science **340**(6130), 286–287 (2013).
40. M. Z. Alam, I. D. Leon, and R. W. Boyd, "Large optical nonlinearity of indium tin oxide in its epsilon-near-zero region," Science **352**(6287), 795–797 (2016).
41. B. C. Yildiz and H. Caglayan, "Epsilon-near-zero media coupled with localized surface plasmon modes," Phys. Rev. B **102**(16), 165303 (2020).
42. S. Suresh, O. Reshef, M. Z. Alam, J. Upham, M. Karimi, and R. W. Boyd, "Enhanced nonlinear optical responses of layered epsilon-near-zero metamaterials at visible frequencies," ACS Photonics **8**(1), 125–129 (2020).
43. M. H. Javani and M. I. Stockman, "Real and Imaginary Properties of Epsilon-Near-Zero Materials," Phys. Rev. Lett. **117**(10), 107404 (2016).

Optics EXPRESS

44. A. Alù, M. G. Silveirinha, A. Salandrino, and N. Engheta, "Epsilon-near-zero metamaterials and electromagnetic sources: Tailoring the radiation phase pattern," Phys. Rev. B **75**(15), 155410 (2007).
45. I. Liberal, M. Lobet, Y. Li, and N. Engheta, "Near-zero-index media as electromagnetic ideal fluids," Proc. Natl. Acad. Sci. **117**(39), 24050–24054 (2020).
46. N. Kinsey, C. DeVault, A. Boltasseva, and V. M. Shalaev, "Near-zero-index materials for photonics," Nat. Rev. Mater. **4**(12), 742–760 (2019).
47. M. G. Silveirinha and N. Engheta, "Theory of supercoupling, squeezing wave energy, and field confinement in narrow channels and tight bends using ε near-zero metamaterials," Phys. Rev. B **76**(24), 245109 (2007).
48. Y. Jing, J. Xu, and N. X. Fang, "Numerical study of a near-zero-index acoustic metamaterial," Phys. Lett. A **376**(45), 2834–2837 (2012).
49. Y. Li, B. Liang, Z.-M. Gu, X.-Y. Zou, and J.-C. Cheng, "Unidirectional acoustic transmission through a prism with near-zero refractive index," Appl. Phys. Lett. **103**(5), 053505 (2013).
50. L.-Y. Zheng, Y. Wu, X. Ni, Z.-G. Chen, M.-H. Lu, and Y.-F. Chen, "Acoustic cloaking by a near-zero-index phononic crystal," Appl. Phys. Lett. **104**(16), 161904 (2014).
51. C. Shen, Y. Xie, J. Li, S. A. Cummer, and Y. Jing, "Asymmetric acoustic transmission through near-zero-index and gradient-index metasurfaces," Appl. Phys. Lett. **108**(22), 223502 (2016).
52. I. Liberal and N. Engheta, "Zero-index structures as an alternative platform for quantum optics," Proc. Natl. Acad. Sci. **114**(5), 822–827 (2017).
53. I. Liberal and N. Engheta, "Near-zero refractive index photonics," Nat. Photonics **11**(3), 149–158 (2017).
54. P. Moitra, Y. Yang, Z. Anderson, I. I. Kravchenko, D. P. Briggs, and J. Valentine, "Realization of an all-dielectric zero-index optical metamaterial," Nat. Photonics **7**(10), 791–795 (2013).
55. J. Xu, X. Deng, H. Zhang, C. Wu, M. Wubs, S. Xiao, and L. Shen, "Ultra-subwavelength focusing and giant magnetic-field enhancement in a low-loss one-way waveguide based on remanence," J. Opt. **22**(2), 025003 (2020).
56. D. M. Pozar, *Microwave Engineering* (John wiley & sons, 2011).
57. X. Deng, L. Hong, X. Zheng, and L. Shen, "One-way regular electromagnetic mode immune to backscattering," Appl. Opt. **54**(14), 4608–4612 (2015).
58. J. Shi, X. Qing, and Z. N. Chen, "Electrically Large Zero-Phase-Shift Line Grid-Array UHF Near-Field RFID Reader Antenna," IEEE Trans. Antennas Propag. **62**(4), 2201–2208 (2014).
59. Y. Zeng, Z. N. Chen, X. Qing, and J.-M. Jin, "A Directional, Closely Spaced Zero-Phase-Shift-Line Loop Array for UHF Near-Field RFID Reader Antennas," IEEE Trans. Antennas Propag. **66**(10), 5639–5642 (2018).
60. Q. Shen, L. Shen, W. Min, J. Xu, C. Wu, X. Deng, and S. Xiao, "Trapping a magnetic rainbow by using a one-way magnetostatic-like mode," Opt. Mater. Express **9**(11), 4399–4408 (2019).
61. J. Luo and Y. Lai, "Hermitian and non-hermitian dirac-like cones in photonic and phononic structures," Front. Phys. **10**, 845624 (2022).
62. Y. Li, C. T. Chan, and E. Mazur, "Dirac-like cone-based electromagnetic zero-index metamaterials," Light: Sci. Appl. **10**(1), 203 (2021).
63. J. Luo, B. Liu, Z. H. Hang, and Y. Lai, "Coherent perfect absorption via photonic doping of zero-index media," Laser Photonics Rev. **12**(8), 1800001 (2018).
64. I. Liberal, A. M. Mahmoud, Y. Li, B. Edwards, and N. Engheta, "Photonic doping of epsilon-near-zero media," Science **355**(6329), 1058–1062 (2017).
65. W. Ji, J. Luo, and Y. Lai, "Extremely anisotropic epsilon-near-zero media in waveguide metamaterials," Opt. Express **27**(14), 19463–19473 (2019).